Computational design and manufacturing of a half-scaled 3D-printed stainless steel diagrid column

Vittoria Laghi, Michele Palermo, Giada Gasparini, Tomaso Trombetti

Computational design and manufacturing of a half-scaled 3D-printed stainless steel diagrid column

In: Additive Manufacturing, volume 36, 2020

The final published version is available online at:

https://doi.org/10.1016/j.addma.2020.101505

Computational design and manufacturing of a half-scaled 3D-printed stainless steel diagrid column

Vittoria Laghi[1]*, Michele Palermo Ph.D[1], Giada Gasparini Ph.D[1], Tomaso Trombetti Ph.D[1]

*corresponding author: vittoria.laghi2@unibo.it

[1]Department of Civil, Chemical, Environmental and Materials Engineering (DICAM) - University of Bologna, Viale del Risorgimento, 2 – 40136 Bologna, Italy

Abstract

The manufacturing of large scale structures with Additive Manufacturing (AM) represents one of the main challenges facing the construction industry today. The first recent large-scale realizations with the Wire-And-Arc Additive Manufacturing (WAAM) technology have shown the potential of WAAM in changing the way steel structures are currently designed and manufactured. However, despite these pioneering applications, the full comprehension of synergies and possibilities of WAAM in terms of architectural shapes, structural behavior and material response are far from being completely exploited.

In this research, the overarching design process from concept to fabrication of a half-scaled diagrid column 3D printed with WAAM technology is illustrated. The research methodology is based on a computational workflow integrating various aspects such as material properties, manufacturing features and global architectural design. The final designed WAAM-produced diagrid column has been exposed at “The Big 5 - International Building and Construction” show, held in Dubai from November 25th till November 28th 2018.

Key words

Directed Energy Deposition; Wire-and-arc Additive Manufacturing; Stainless steel; Experimental tests; Digital fabrication.

1. Introduction

Along the centuries, the evolution in building construction has always been strictly linked to significant advancements in material science, technology, industrial processes and engineering [1]. During the last 30 years, the way structures have been designed, planned and built changed completely following the technological innovations offered by software for Computer-Aided Design (CAD), which replaced manual drawings, without however, at the beginning, changing the resulting architectural shapes. In the early years of the 21st century, a new design approach in architecture started to emerge resulting in novel forms thanks to the introduction of three-dimensional computer modelling and digital fabrication methods. More recently, with the advent of the "digital turn" [2], novel computerized tools for architecture, structural and civil engineering have gained influence, enabling the design and construction of buildings with complex, doubly-curved geometry, such as shell structures and other forms found through design optimization [3].

Since the beginning of 21st century, automation has grown exponentially and soon prevailed in almost all production domains with the exception of the building construction sector, in which the use of automation is still challenging and at its pioneering applications, due to some peculiar aspects proper of the construction industry. These aspects lie within the large-scale dimensions of the products, the conventional design approaches which are not fully suitable for automation, as well as limitation in the materials to be employed by an automated system [4]. Only in the last few years, the fast development in digital fabrication techniques is leading towards applications in structural engineering field as well, through Additive Manufacturing (AM)-based technologies, already commonly used in other sectors such as aerospace, automotive and biomedical engineering [5–9].

The application of Additive Manufacturing (AM) process in the built environment allows to exploit the innovations in architectural forms from digital design tools to create new forms and shapes. The first investigations have been carried out on polymer-based AM techniques. Naboni et al. [10] exploited 3D printing technology to create a polymer-based cellular trabecular pavilion currently exposed at Politecnico of Milan. New possibilities towards the application of 3D printing technology for large-scale building parts in polymers have been also explored by Branch Technology [11] and AI Build [12]. Concerning concrete direct 3D printing, there is several research effort as well as building applications already present in the market. Some interesting studies and applications of structural optimization for new classes of 3D printing concrete elements have been developed by Vantyghem et al. [13], as well as by ETH Zurich research team [14].

As far as metal-based AM processes applied to construction field, Powder-Bed Fusion (PBF) techniques allow to print small elements, therefore adapted for small steel connections, as for the case

of the optimized node presented by ARUP [15]. However, the most suitable AM process for steel structures results to be the so-called Wire-and-Arc Additive Manufacturing (WAAM), which consists of standard welding equipment mounted on top of a numerically-controlled robotic arm. It allows for a relatively fast (when compared to other AM processes) realization of members of large dimensions (up to few meters span), with ideally almost no limitations in the size or shape, for the construction of innovative architectural forms.

In this regard, the first example of optimized shape manufactured using WAAM process is the MX3D Bridge [16], the first 3D-printed steel footbridge ever realized, presented and awarded at the Dutch Design Week held in Eindhoven in October 2018 (Figure 1). The bridge is ready to be installed in Amsterdam city center by 2020. Other explorations on the applications of WAAM process for innovative structural elements have been also carried out at University of Technology Darmstadt [17].

Figure 1: MX3D Bridge realized with WAAM process [16].

Nonetheless, further research effort is still required to completely characterize the geometrical and mechanical features of the process outcomes in terms of surface roughness and imperfections with respect to the digital input as well as mechanical and microstructural properties of WAAM steel members. Indeed, the results in literature focusing on the microstructural and mechanical characterization of different alloys realized by means of WAAM process [11–43], indicate that the mechanical properties of WAAM material may differ from those of the corresponding wrought one. However, there is still limited research specifically focused on the characterization of WAAM-produced metal elements for structural engineering applications [51].

Recently, the authors carried out a wide experimental campaign to assess the geometrical, mechanical

and microstructural properties of WAAM-produced 308LSi stainless steel elements to be applied in the structural engineering field [52–54].

The present study illustrates the overarching process, as the whole comprehensive process from computational design to fabrication adopted to realize a stainless steel diagrid column realized with WAAM technology. The computational design workflow integrates various aspects such as material properties, manufacturing features and global architectural design. It includes both conceptual and parametric design. The diagrid column is made by "rods" (as diagonal elements) realized in 3D-printed stainless steel using a so-called "dot-by-dot" printing strategy. Section 3 presents the main results of the geometrical and mechanical characterization of the dot-by dot rods produced with WAAM technology. Sections 4 and 5 present the computational design process, from the concept to parametric design and fabrication of the designed diagrid column.

The designed column is intended as a showcase to highlight the potential of metal 3D printing technology to realize innovative structural forms and aesthetically appealing architectures (Figure 2).

Figure 2: futuristic application of a 3D-printed diagrid column.

2. Wire-and-Arc Additive Manufacturing in construction: issues and possibilities

The specifications of WAAM process parameters and the knowledge of their effects on the geometrical and mechanical properties of the printed outcomes are crucial for a reliable evaluation of the structural behavior of the whole printed structure [25,30,35,44,55–59]. Up to date, the main source of uncertainty is the AM process itself, as the outcome of the printing process is a metal material with

geometrical features and mechanical properties that may substantially differ from those of traditionally fabricated elements.

Among different WAAM set-up configurations, hereafter the printing process currently adopted by the MX3D company [16] is considered. In detail, two different printing strategies have been explored so far: a so-called “continuous” printing, meaning that the material is deposited in continuous, and a so-called “dot-by-dot” printing, meaning that the material is deposited by successive points. Typically, “continuous” printing is adopted to print planar elements, while “dot-by-dot” strategy is used to print line elements as parts of a continuous diagrid pattern, with no nodes interruptions. The effects of these strategies on the metallurgic characteristics of the printed material have been recently analyzed in [45,60–62].

The fundamental process parameters are (i) the current and its voltage, (ii) the wire diameter, (iii) the wire-feed rate, (iv) the welding speed and (v) the vertical printed layer height. The combination of such controlling parameters affects the printing quality (geometrical precision and surface roughness) and the material mechanical properties [55,57–59]. In addition, different cooling strategies (such as active cooling system or natural ambient cooling) may influence the mechanical properties and therefore should be considered [35].

For structural engineering applications, the need of high welding velocity for a rapid realization of structural elements of such proportions plays a crucial role for the specific characteristics of the printed parts, as it causes geometric defects in the outcomes, both in terms of surface roughness and lack of straightness of the elements. For a given element to be printed, a digital model, from which the printing head reads the coordinates of the points defining step by step the position of the welded layer, is created with Rhinoceros software [63]. However, due to the intrinsic inaccuracy of the printing process, the printed member will differ from its ideal digital counterpart. Moreover, the surface roughness caused by the layer-by-layer deposition system causes an anisotropic behavior from both the microstructural and mechanical point of view [52,53].

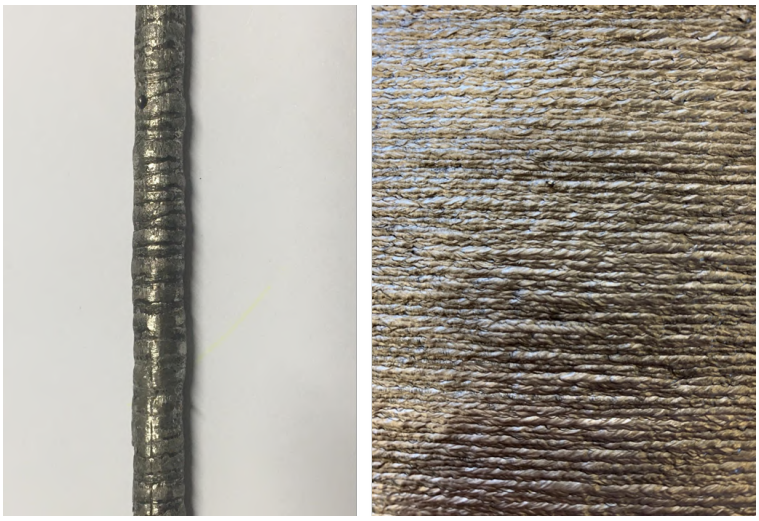

(a) (b)

Figure 3: the inherent surface roughness of the WAAM printed outcome: (a) dot-by-dot printing; (b) continuous printing.

3. Material characterization of dot-by-dot elements

3.1 The printing process

The printing strategy considered for the design of both the specimens tested and the diagrid column is the so-called "dot-by-dot". In detail, the "dot-by-dot" printing strategy is a Wire-and-Arc Additive Manufacturing technique to deposit dots of welding metal on a discontinuous process along one axis [61,62]. The printed outcome results in a one-dimension rod-like element, having constant nominal diameter (as governed by the welding dot) and longitudinal main axis. The specimens have been manufactured by MX3D company [16] using a commercially available standard stainless steel welding wire grade ER308LSi (1 mm diameter) supplied by *Oerlikon* [64]. The printing parameters are listed in Table 1. Since the "dot-by-dot" printing strategy is a discontinuous process, travel speed has not been set within the process parameters.

Process parameters	**Details**	**Value**
Deposition power	Current	100 - 140 A
	Arc voltage	18 - 21 V
Speed	Welding spot	0.5 - 1 s
	Wire feed rate	2 - 4 m/min
Distance and angle	Rod diameter	3- 7 mm
	Electrode to layer angle	90°

Wire	Wire grade Wire diameter	ER 308LSi 1 mm
Shield gas	Shield gas type Shield gas flow rate	98% Ar, 2%CO_2 10-20 L/min

Table 1: Printing process parameters.

In order to study the mechanical behavior of WAAM-produced "dot-by-dot" elements, tensile and compression tests have been conducted on 6-mm diameter full circular rods including tests. The rods have been produced in two orientations: (i) with the longitudinal axis aligned along the vertical direction, coincident with the printing direction; (ii) with the longitudinal axis inclined by an angle of 10° with respect to the vertical direction (Figure 4) to evaluate the influence of a possible misalignment of the printing head from the longitudinal axis of the printed element.

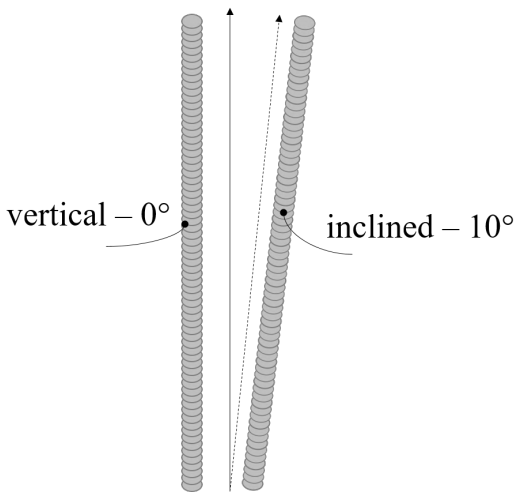

Figure 4: The two orientations of the specimens tested: vertical (aligned with the vertical direction of deposition) and inclined (at 10° from the vertical direction of deposition).

A total number of 40 specimens have been tested, 20 per each direction, to fully characterize the geometry and the mechanical response of the printed outcomes. First, a detailed geometrical characterization has been performed, making use of a high-precision 3D scanning acquisition system (Section 3.2). Then, tensile and compression tests have been performed on the specimens (Section 3.3) to evaluate the main material properties to be used in the computational design phase (Section 4).

3.2 The geometrical characterization

Given the inherent surface roughness of the WAAM-produced rods, high-precision 3D scanning acquisition has been adopted to evaluate the distribution of cross-sections with respect to the digital input. Indeed, the rods have been realized having a full circular cross-section of nominal diameter equal to 6 mm. Figure 5a presents the comparison of the 3D model of a printed rod obtained from 3D scanning acquisition (blue) and the corresponding nominal geometry of a uniform cylinder (red) of 6-mm nominal diameter (taken as input digital model during the printing phase). The 3D model obtained from the laser scanner clearly evidences the three main types of discrepancies: irregular cross-section along the length, surface roughness and lack of straightness. As a result, the nominal cylinder (red) is visible above the real one (blue) not only because of the difference in cross-section, but also due to the presence of lack of straightness as global imperfections.

Figure 5b shows the distribution of the diameter as evaluated on 100 cross-sections of the 3D-scan model (in terms of relative frequency scaled to have a unitary bars area) and the Gaussian Normal probability density function (PDF) which fits best the distribution of the diameter measures.

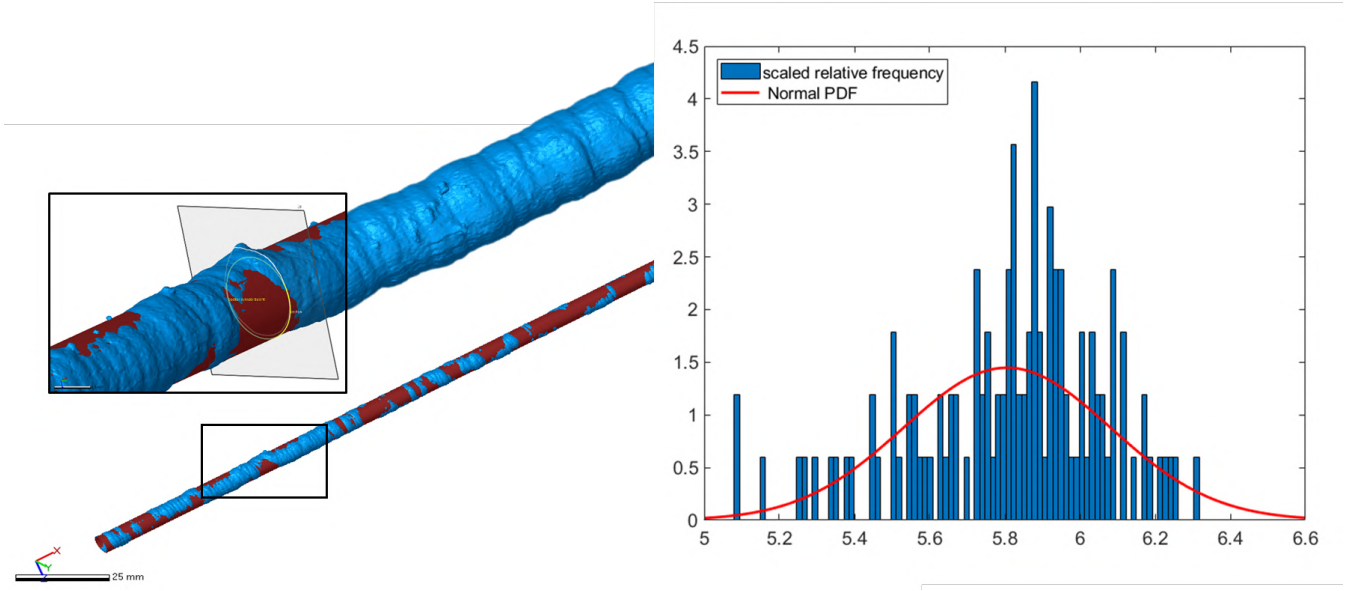

(a) (b)

Figure 5: (a) 3D-scan model vs. digital input geometry; (b) distribution of diameter of a WAAM-produced rod.

The average diameter resulting from the analysis of the 3D-scan acquisition is equal to 5.81 mm, resulting in a discrepancy with respect to the nominal value of 3%. The coefficient of deviation results equal to 0.28. These values are also in line with the results of previous investigations carried out by the authors on WAAM-produced continuously-printed stainless steel specimens [52,54].

In order to correctly interpret the results of the mechanical tests, a volume-equivalent effective cross-section has been considered as the resistant effective area adopted to compute the effective stresses from tensile tests, according to the procedure presented in [52]. Indeed, the effective stresses provide an estimation of true stress in a WAAM-produced specimen that could be useful for structural design purposes [52]. The values of the effective cross-sectional area have been taken from volume measurements according to Archimedes' principle. The average value of the effective diameter taken over the 40 specimens is 5.80 ± 0.27 mm, substantially equal to the average diameter obtained from 3D-scan acquisition. Note also that the difference between the effective diameter and the nominal one is in the order of 3% of the nominal value.

3.3 The mechanical characterization

The tensile tests have been performed on a Universal testing machine of 500 kN load capacity at the Structural Engineering labs of University of Bologna. The specimens have been tested in displacement-control with a velocity of 2 MPa/sec. Two types of monitoring systems have been adopted to evaluate the strains: a linear deformometer of nominal dimension of 50 mm, to detect the linear deformation of the specimens up to yielding, and an optical-based system referred to as Digital Image Correlation (DIC), to acquire the full strain field during the whole test until failure (Figure 6). Figure 7 shows an overview of the mechanical test results in terms of average values and standard deviation of Young's modulus (E), 0.2% proof stress ($R_{p0.2}$), ultimate tensile strength (UTS), elongation to failure ($A_{\%}$). The same information is collected in Table 2 including also the strength ratio ($R_{p0.2}/UTS$). It can be noted that the values of the mechanical parameters are generally in line with the results obtained from the experimental campaign carried out on WAAM-produced continuously-printed stainless steel specimens [52,53]. In detail, the main discrepancy results to be on the 0.2% proof stress values (on average around 250 MPa for dot-by-dot vs. 300 MPa for continuous), which clearly affects the strength ratio as well (around 0.45 for dot-by-dot vs. 0.65 for continuous).

(a) (b)

Figure 6: (a) *Tensile/compression test set-up; (b) typical tensile rupture; (c) typical compression/buckling failure (specimen of aspect ratio around 0.7).*

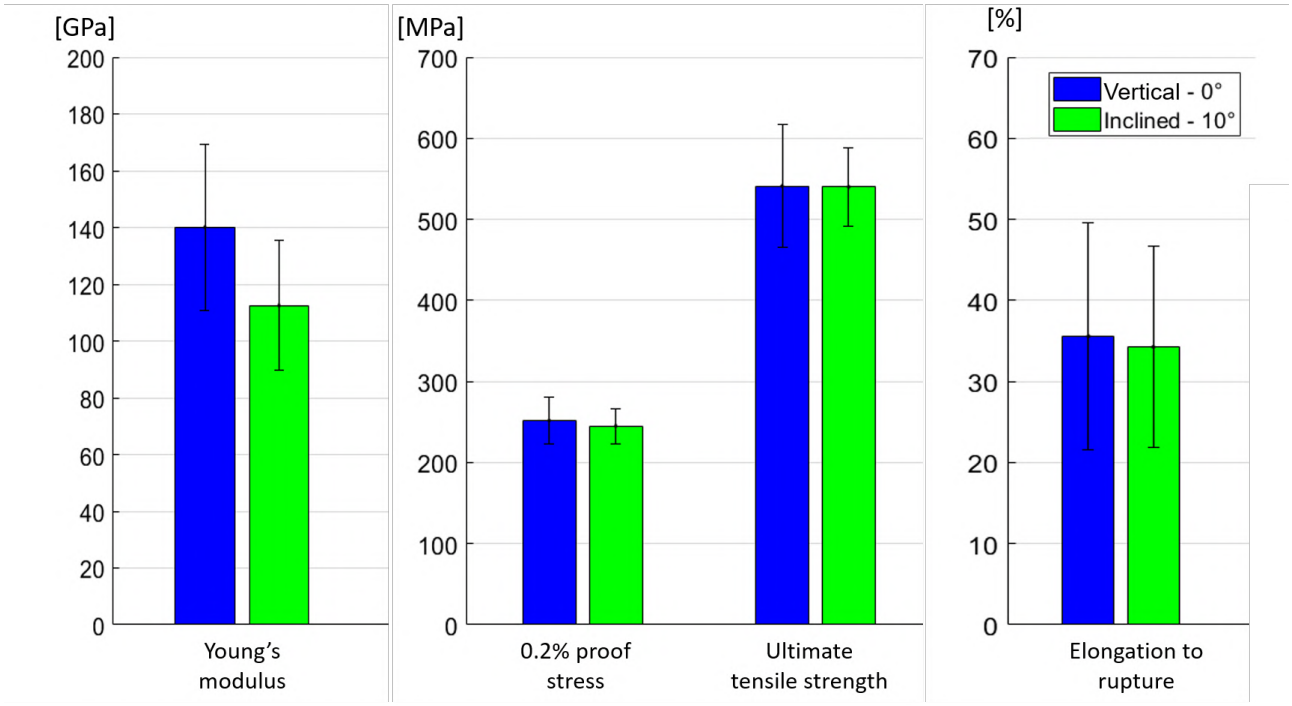

Figure 7: Overview of the mechanical parameters from the tensile tests.

Specimen orientation	E [GPa]	$R_{p0.2}$ [MPa]	UTS [MPa]	$A_{\%}$ [%]	$R_{p0.2}$/ UTS
Vertical – 0°	140.08 ± 29.33	251.86 ± 28.75	527.31 ± 75.78	35.58 ± 13.98	0.47 ± 0.03
Inclined – 10°	112.51 ± 22.91	245.01 ± 21.57	540.10 ± 48.33	34.26 ± 12.37	0.46 ± 0.04

Table 2: Summary of tensile tests results.

Compression tests have been performed on rod-like specimens having different lengths L (slenderness ratios i/L_{eff} from 0.30 to 1.80, with i equal to the cross-section radius of gyration and L_{eff} the effective length based on the end-constraints), using the same experimental set-up as for the tensile tests. The results have been then analyzed to evaluate the critical buckling load (N_{cr}) from which the design buckling curve is interpolated. The results of the compression tests indicate that for the designed diagrid column the use of rods with a maximum free length of 50 mm (corresponding to a slenderness ratio of 0.30) would ensure a compression strength approximately equal to the tensile yielding strength. Therefore, for the design and verification phases (Section 4) the axial resistance under compression of the rods has been considered as follows: $N_{cRd} = N_{tRd} = A_{eff} \cdot f_{yd}$. A_{eff} corresponds to the volume-equivalent effective cross-sectional area, while the design yielding strength f_{yd} has been obtained from the results of the tensile tests considering the mean value of the 0.2% proof stress ($R_{p0.2}$) and corresponding partial factor according to provisions in Eurocode 3 for structural members realized in stainless steel material [65].

4. Computational design of the diagrid column

The present section illustrates the computational design process (from the concept to the final design) of a WAAM-produced diagrid column. The conceptual design has been guided by solutions found in the scientific and technical literature (Section 4.1) dealing with the problem of determining the optimal shape of a structural element subjected to compression. The parametric design phase, presented in Section 4.2, has been carried out in two steps, namely the global shape design and the topological design, and takes into account the manufacturing constraints and the material properties of the adopted WAAM process, thus allowing to obtain the final design ready to be 3D-printed

without the need of further iterations. The structural performances of the final design are evaluated by means of finite element analysis comparing the stress levels with that of a benchmark solution (Section 4.3).

4.1 Historical precedents

Since Galileo Galilei's investigations on "equistrong beams" in the 17th century, several researchers have been dedicated an effort on determining the "most efficient shape" of an element, intended as the configuration of minimum weight ensuring the same safety factor under certain applied loads and restraint conditions. The shape of the equistrong rod under a compressive force is found in the Euler's problem. In 1960 Keller [66] solved the problem of determining the shape of a column with the largest critical buckling load, of a given length and volume. The results show that the strongest column is not uniform but tapered, being thicker at its center and thinner at its ends. Indeed, appropriately tapering a column of circular cross-section increases its critical buckling load by one-third over that of a uniform column. The analytical equation of the along-the height variation of the cross section area of the strongest column has a quadratic sinusoidal form [66]. Such a column with variable cross section has a weight reduced by 13% of that of a uniform full cylindrical column having the same buckling load [67].

In addition to the theoretical studies related to the strongest beam, more practical-oriented research has been carried out since the early 20th century to obtain efficient structural solutions for tall and slender structures, such as nuclear cooling towers or water towers. In particular, hyperboidal thin shell structures are characterized by excellent aerodynamic, strength and stability properties. The remarkable Russian engineer Vladimir Shukov, who designed and realized the hyperboloidal water tower for the 1896 industrial exhibition in Nizhny Novgorod, is recognized as the pioneer of hyperboloidal structures. More recent examples of hyperboloidal structures are the McDonnell Plantarium roof in St. Louis, the Brasilia Cathedral and the Kobe Port tower [68]. As hyperboloid structures are doubly curved, their simultaneous curvature in opposite directions leads to high resistance against buckling. Furthermore, given their anticlastic curvature, they are able to carry the same load with less amount of material with respect to traditional cylindrical shapes [69,70].

The two families of optimal shapes for a column subjected to compression, namely the "sinusoidal-like" and the "hyperbolic-like", have been considered in this study as selection criterion to identify the global geometrical shape of the diagrid column in the first step of the parametric design process (Section 4.2). Figure 8 conceptually explains the merging of the "sinusoidal-like" and "hyperdoloic-like" shapes towards the the final designed shape.

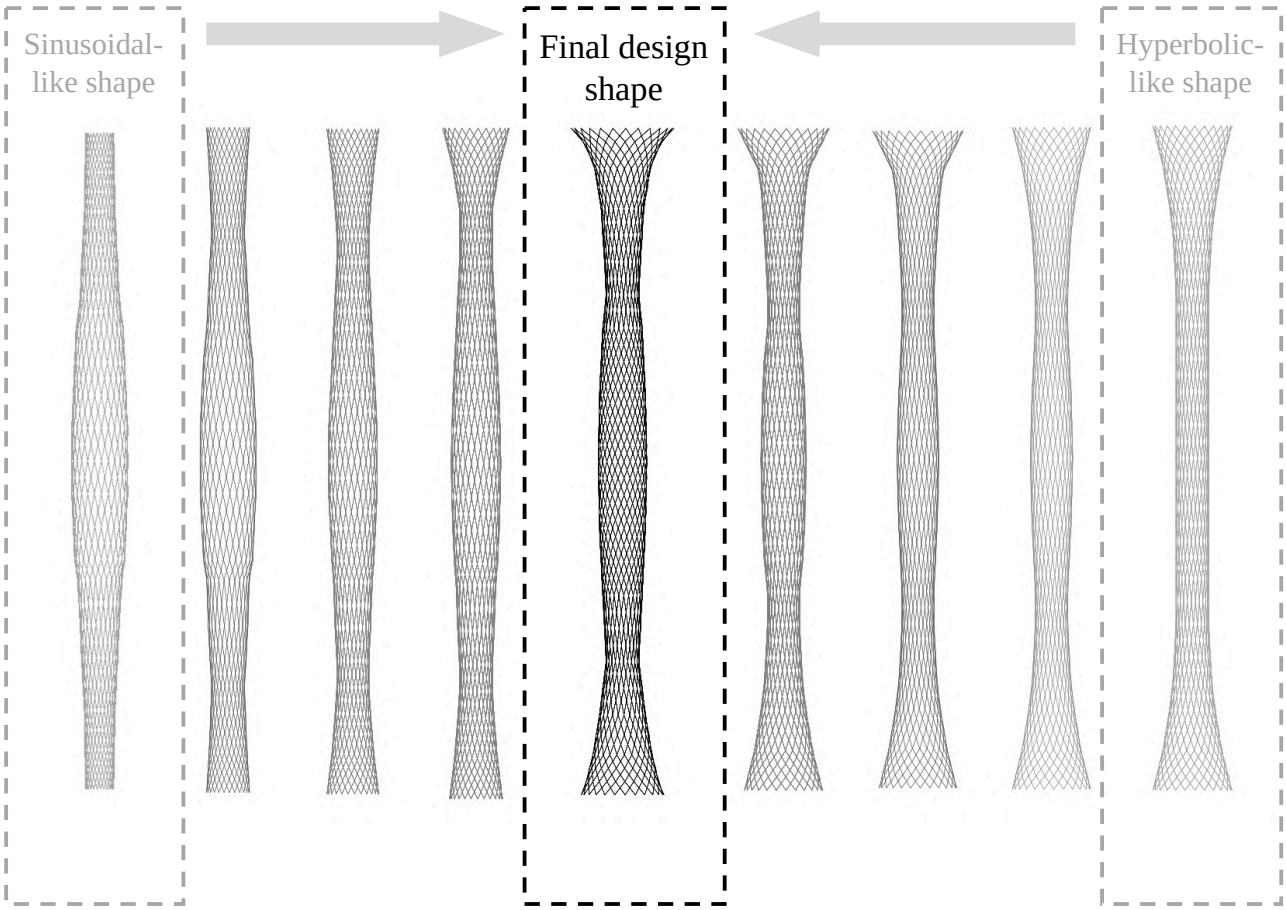

Figure 8: Path towards the shape of a diagrid column.

4.2 The parametric design algorithm

The computational design flow is articulated in different phases (Figure 9), from the set of the initial geometry (phase 1) to the parametric design algorithm (phase 2 and 3) towards the final design. In detail, the parametric design phases are the global shape design (phase 2) and the topological design (phase 3). In both parametric design phases, a parametric design algorithm has been implemented by means of *Grasshopper* [71] program in *Rhinoceros5* [63] software environment, widely used for parametric design purposes since it allows to perform advanced algorithm-aided design and structural analyses directly on CAD drawings through a real-time iterative procedure to the final design. The two plug-ins used for the purpose of the present work are *Karamba3D* [72] and *Galapagos* (built-in feature of *Grasshopper* [71]): the first one, in particular, is a plug-in able to perform non-linear structural analysis of beam and shell models; the second one, instead, solves optimization problems making use of genetic algorithms to generate a population of different solutions based on the problem at hand.

The objective of both global and topological design is to determine the structural configuration (defined in a parametric form) of minimum weight satisfying a target structural requirement under additional constraints. In each design step, specific geometrical parameters are chosen as the design variables, while the remaining ones are set to constant values. The final configuration at the end of each design step is selected among the ones generated by the genetic algorithm according to a selection criterion. The structural requirements are verified through linear static analyses by computing the utilization factors (U_i) of each structural member and verifying U_i <1.0. Indeed, the utilization factor, according to Eurocodes [73], is computed as the ratio between the design actions and the corresponding resistances for a given limit state, and the acceptable design should satisfy the threshold of utilization factor of 100%.

In this case, the utilization factor is calculated as $U = \frac{N_{Ed}}{N_{Rd}} + \frac{M_{y,Ed}}{M_{y,Rd}} + \frac{M_{z,Ed}}{M_{z,Rd}}$, where N_{Ed}, $M_{y,Ed}$ and $M_{z,Ed}$ are respectively the axial force and bending moments along directions y and z due to the applied loads, while N_{Rd}, $M_{y,Rd}$ and $M_{z,Rd}$ are the corresponding resisting values.

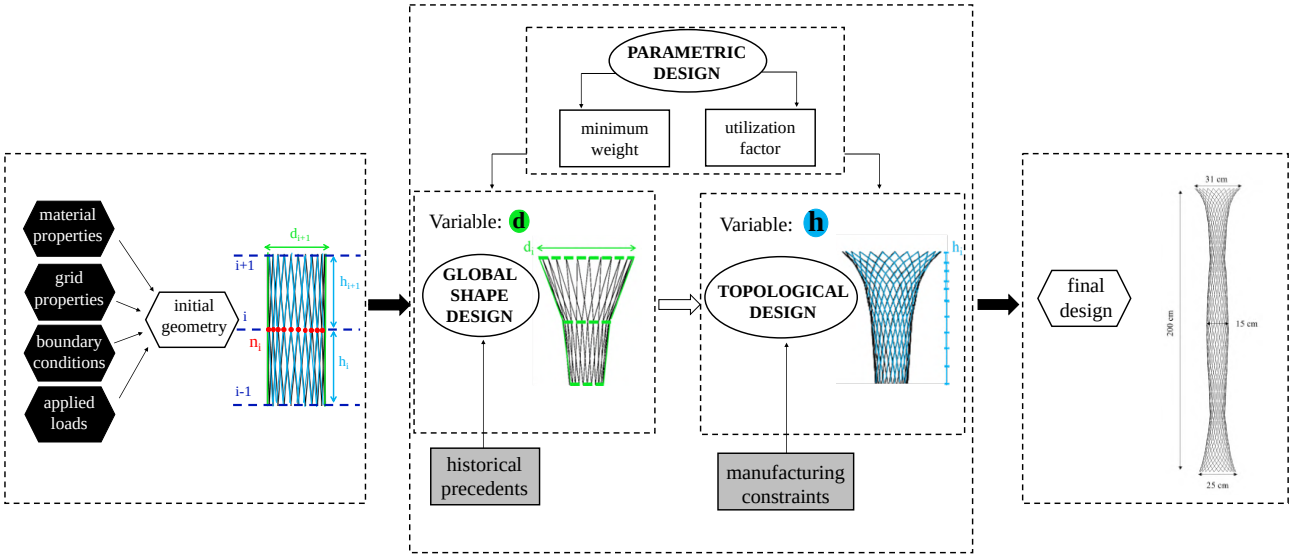

Figure 9: Computational design flowchart.

The first phase consists in the creation of a parametric model considering the following inputs: (i) material properties, (ii) grid properties, (iii) boundary conditions and (iv) applied loads. Based on the specific inputs, an initial geometrical configuration is generated in a parametric form. The parametrization allows to control both the global shape and the topology acting on some of the parameters (Figure 10). In the specific case, the selected geometry is a non-uniform cylindrical diagrid tube described by the following set of parameters (Figure 10a): number of control sections *N*

along the column height (z_i indicates the vertical coordinate of the i-th cross-section), the outer diameter d, the section spacing h (corresponding to the distance between two consecutive control sections) and the number of control points n (from which at each control section the diagonal elements are generated). At the i-th control section it is thus possible to associate specific values of parameters d_i, h_i, n_i.

In phase 2 (global shape design) the GA variable (i.e. variable of the genetic algorithm) is the outer diameter d, governing the external shape of the column. Among the population of allowable solutions found through the algorithm, the selection criterion for the final global shape is based on the "merging" of the two best shapes: the sinusoidal-like and the hyperbolic-like (Figure 10b).

In phase 3 (topological design), the GA variable is the section spacing h, governing the length of the diagonal elements, hence the topology of the diagrid. Among the population of allowable solutions found through the genetic algorithm, the selection criterion for the final topology is based upon the manufacturing constraints proper of the process, in terms of maximum allowable rod lengths l and angle of inclination (θ) of the diagonal elements (Figure 10c).

For both phases, the "fitness value" of the GA (genetic algorithm) corresponds to the minimization of the mean utilization factor, as performed through *Karamba3D* component [72].

At the end of the computational design, the result of the final design is provided in terms of a set of values of the geometrical parameters (d, h, n) for each control section of the column.

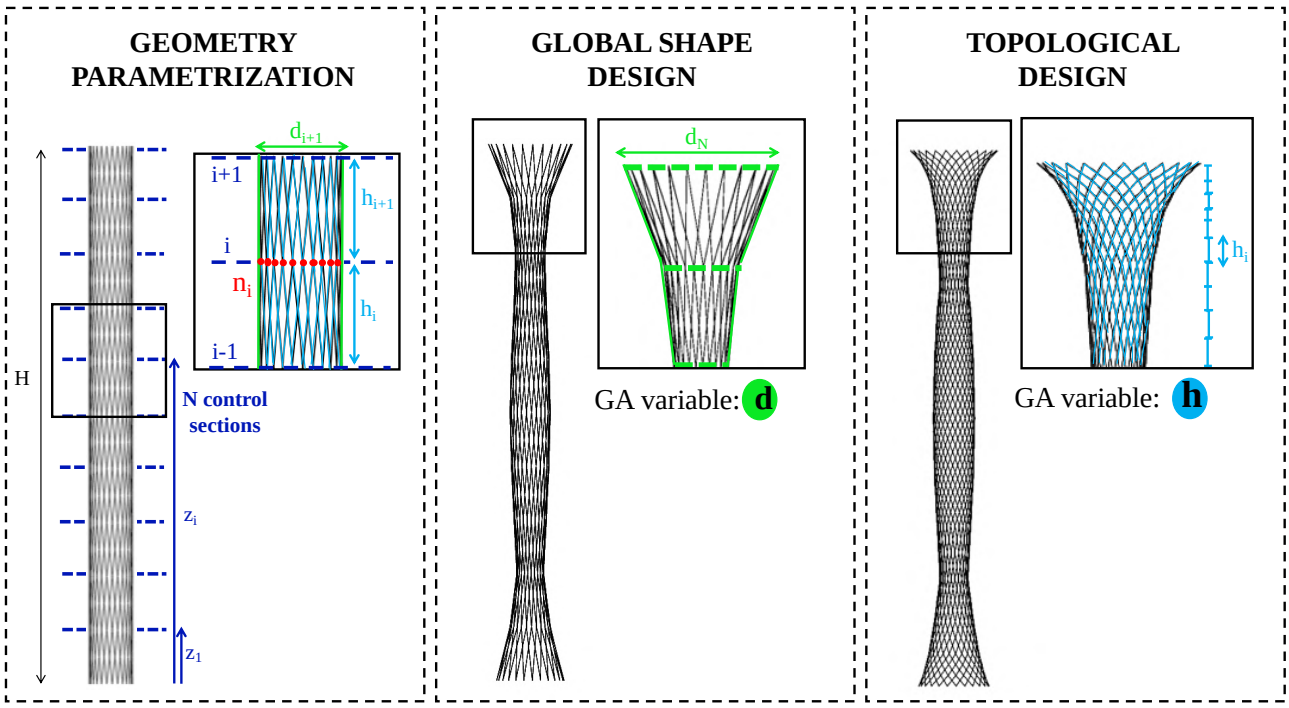

(a) (b) (c)

Figure 10: Phases of the parametric design: (a) parametrization of the geometry; (b) global shape design; (c) topological design.

4.3 Design of the diagrid column and its global performances

A 2 m-high WAAM diagrid column has been designed according to the parametric design algorithm presented in Section 4.2. The design is a half-scaled structure representative of a 4-m high column. The assumed initial geometrical configuration at phase 1 is characterized by a constant diameter d=15 cm at all control sections. The inclined rods of the diagrid have a 6-mm diameter. The design is developed considering a reference vertical load of 25 kN applied at the top of the column. The applied vertical load corresponds to the resultant of distributed loads simulating the loads (dead plus live) applied on top of a porticos-like structure. It is assumed that the 1:1 scaled column would withstand the loads applied on an influence area corresponding to a 5-m column spacing. The column is considered clamped at the base, while the top is free to translate and rotate (cantilever condition). The mechanical properties of the rods (Young's modulus, tensile and compression capacity) are taken from the results of the experimental tests on dot-by-dot WAAM specimens described in Section 3.3. In phase 2 (global shape design), the sections spacing h and number of control points n have been set constant and equal to 20 cm and 25 at each section, respectively. The along-the-height distribution of the external diameter $d_i(z_i)$ at each control section defines the global shape of the diagrid. The values d_i have been obtained from the population of allowable solutions coming from the genetic algorithm, according to the shape criterion, as a linear combination of the two "optimal shape functions". The values of d_i vary from 10 cm to 31 cm with an average value of 16 cm (Figure 11a).

In phase 3 (topological design), the number of control points n has been set constant and equal to 25 at each section, while the distribution of external diameter $d_i(z_i)$ is based upon the result of phase 2. The cross-section spacing $h_i(z_i)$ defines the global topology of the diagrid. The values h_i have been determined from the population of allowable solutions coming from the generic algorithm and accounting for the manufacturing constraints: maximum rod lengths $l \leq 100$ mm and maximum angle $\theta \leq 30°$ (Figure 11b). In particular, by changing the section spacing h, a higher number of control sections N resulted to define the final design while following the manufacturing constraints. Figure 11b compares the initial topology (having 10 control sections and constant cross-section spacing h equal to 20 cm) with the final one (having 35 control sections and cross-section spacing h_i varying from 4 to 10 cm). The final diagrid column is presented in Figure 11c.

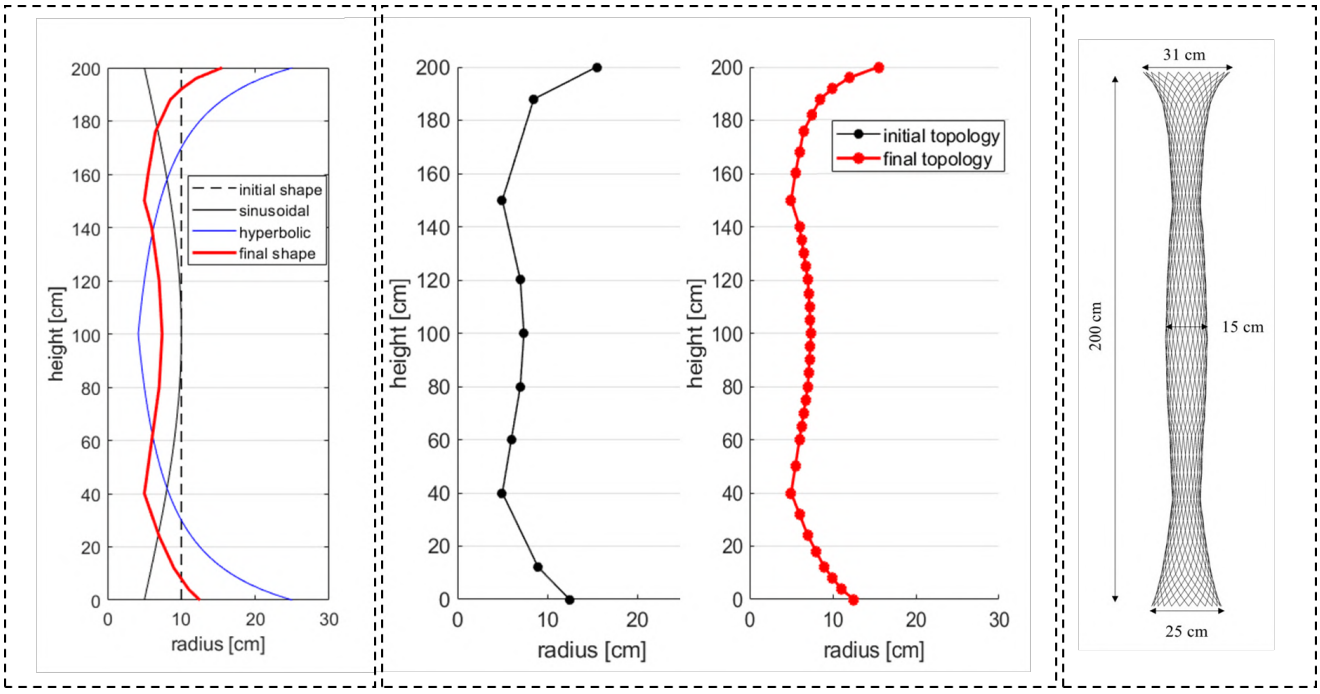

(a) (b) (c)

Figure 11: Diagrid parametric design: (a) global shape design; (b) topological design; (c) the final design.

For the sake of comparison, a uniform (constant diameter along the height) cylindrical diagrid column has been also designed. The equivalent cylindrical diagrid column is characterized by the following geometrical parameters: constant outer diameter (d=20 cm), constant sections spacing (h=20 cm) and constant number of control points (n=30). The rods have a 6-mm diameter. The cylindrical diagrid column has been designed to have maximum utilization factor $U_i \leq 100\%$ under the same vertical load of 25 kN.

The structural performances of the two diagrid columns have been evaluated by means of FE analyses carried out with the commercial software SAP2000 [74]. In particular, linear static analyses have been conducted with the purpose of evaluating the stresses in the diagrid members due to a constant vertical load of 25 kN. Each rod is modelled with a unique beam element having circular cross-section of 6 mm diameter. The total vertical load is applied through concentrated vertical forces applied at the top nodes.

A rigid hoop (not present in the original design) is added at the level of the top nodes of the two columns in order to limit the bending stresses at the top and account for practical issues of load application, thus ensuring better structural performances. The top horizontal hoop is not part of the computational design as the manufacturing constraints proper of the studied WAAM dot-by-dot printing strategy do not allow to print horizontal elements. However, it could be easily manufactured

separately (even using more traditional techniques) and then welded after the completion of the column.

In order to evaluate the effectiveness of the proposed solution with respect to the uniform cylinder, two global performance indices have been introduced: the weight ratio (weight of the final design divided by the weight of the uniform cylinder) and the average utilization ratio (mean utilization factor of the final design divided by the mean utilization factor of the uniform cylinder). The mean utilization factor corresponds to the average value of the utilization factor along all members.

Table 3 reports and compares the two designs in terms of weight and utilization factor. The values of the weight ratio (0.88) and utilization ratio (0.72) indicate that the proposed solution is more efficient than the cylindrical column in terms of both amount of material and average utilization. It is worth noticing that the utilization factors of both solutions have a large variability from the minimum to the maximum values, which will be further discussed in the next section.

	Weight (W)		**Utilization factor (U)**			
	W	**W_{final} / $W_{uniform}$**	**U_{min}**	**U_{max}**	**U_{mean}**	**$U_{mean,final}$ / $U_{mean,uniform}$**
Uniform cylinder	26.87 kg	0.88	29%	86%	68%	0.72
Final design	23.66 kg		14%	75%	49%	

Table 3: Global Performances of the two solutions in terms of weight ratio and utilization factors.

4.4 Effects of the computational design on the structural performances of the diagrid column

In this section the structural behavior of the two compared solutions is analyzed. In general, for both solutions, the absence of horizontal hoops at the level of the control sections determines the presence of an unbalanced component (outward "centrifugal" force as depicted in Figure 12) of the internal actions at the intersection of two rods responsible for secondary bending moments which substantially increase the stresses in the diagonal rods. This behavior is known in the structural engineering design of tall buildings [75–78] which make use of structural diagrid, such as 30 St. Mary Axe in London (Figure 13). Indeed, most of the diagrid-based designs in architecture include horizontal elements (working as "hoops") to contain and prevent the previously mentioned unbalanced forces. However, there are few examples (as it is the case of the QIPCO Tower in Doha, the Prada Ayoama building in Tokyo and of the Oakland Arena) in which the structure performs without any horizontal hoop closing the diagrid (Figure 13b).

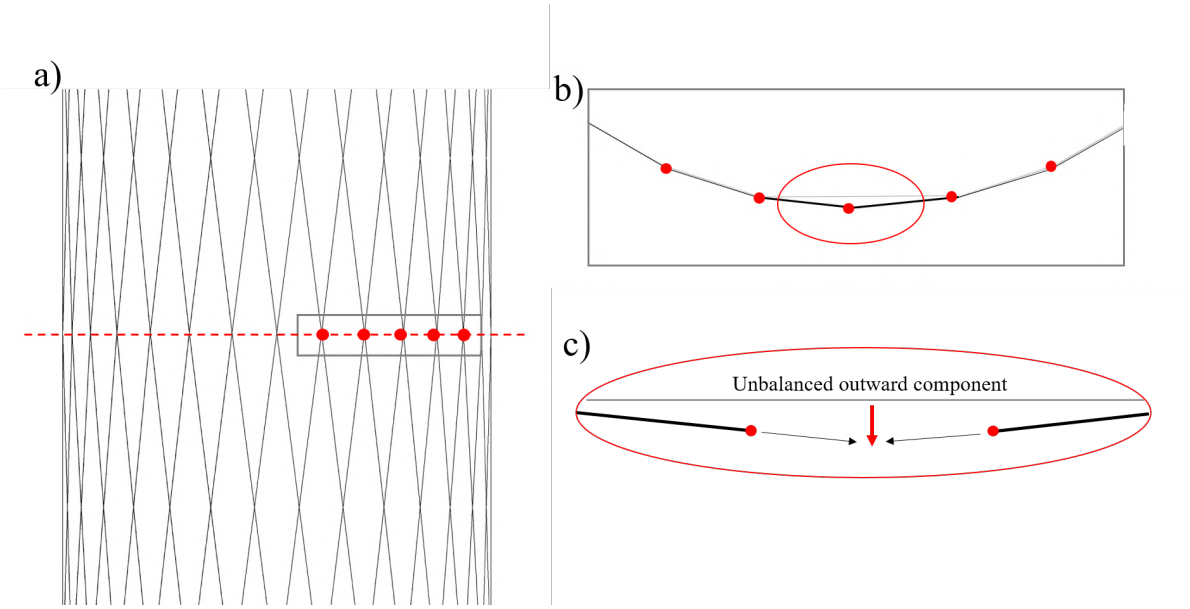

Figure 12: Geometrical considerations on unbalanced "centrifugal" actions on the diagrid column: (a) side view; (b) plane view; (c) close-up.

(a) *(b)*

Figure 13: Typical examples of diagrid structures applied to tall buildings: (a) 30 St. Mary Axe; (b) QIPCO Tower.

Figure 14 represents the bending moment diagrams and the distributions of the utilization factors along the height of the two compared solutions. The uniform cylinder presents an almost symmetrical

(with respect to the mid-height) along-the-height distribution of the bending moments and utilization factors with maximum values around the mid height and minimum values at the top and bottom portions. This reduction in bending moment (and utilization factor) is due to restraining effects provided by the upper hoop and the base connection.

On the other hand, the final design results in a non-symmetrical along-the-height distribution of bending moments and utilization factors, due to the continuously changing curvature associated to the global shape partially contrasting the "centrifugal" outward actions due to the absence of horizontal hoops as evidenced in Figure 12. Overall, the peak values of bending moments (and utilization factors) are lower than those of the uniform cylinder.

Figures 15a and b present the cumulative graphs and relative frequency histograms of the utilization factors for the two designs. The comparison between the cumulative graphs clearly shows that the final design leads to reduced values of the utilization factors. For the case of the uniform cylinder column, the histogram of the relative frequency shows that the U values are grouped into two main ranges, one around 0.3-0.4 and one around 0.7-0.9, with a peak in the range of 0.8-0.9. On the other hand, for the final design the U values are more uniformly distributed with values between 0.2 and 0.8 .

This result suggests future possibilities for more efficient designs of the diagrid column, towards a more uniform along-the-height distribution of utilization factors. This could be done in principle by changing the thickness of the rods. However, at the current state of art of WAAM applications it is not a feasible solution for the dot-by-dot printing strategy.

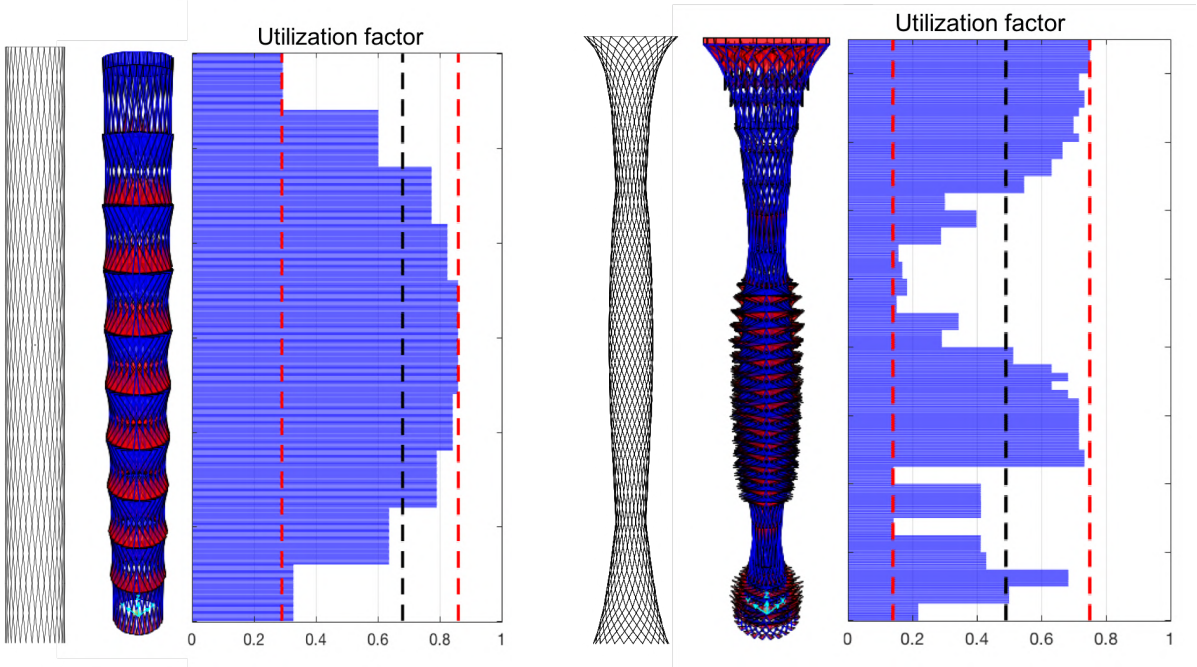

(a) (b)

Figure 14: Results from structural analysis in terms of bending moment diagram and utilization factor: (a) uniform cylinder; (b) final design.

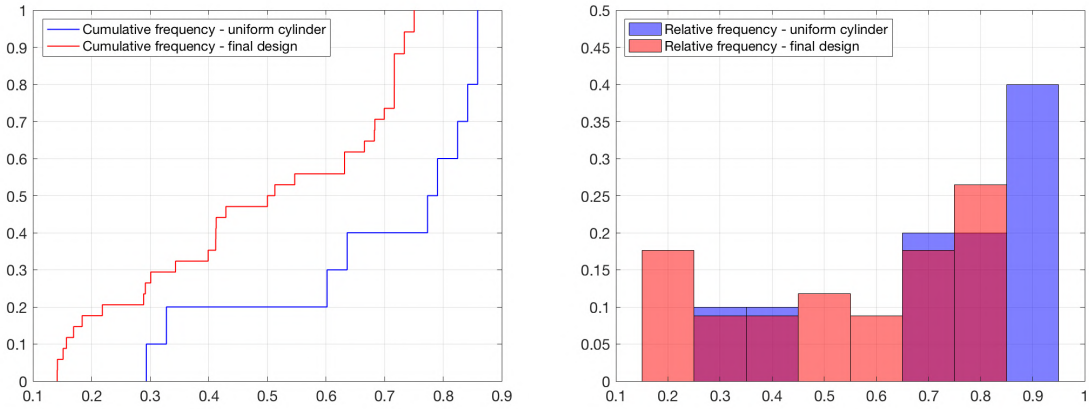

(a) (b)

Figure 15: Distribution of the utilization factors for the two compared solutions; (a) cumulative frequency graph (b) histograms of relative frequency.

5. Fabrication

The final stage of the research consisted in the fabrication of the diagrid column as per the final design, using the WAAM technology adopted by MX3D (Figure 16).

The printing set-up consists of off-the-shelf welding equipment, such as welding power source, torches and wire feeding system, while motion is provided by a numerically-controlled robotic arm. WAAM's layer height is commonly in the range of 1 to 2 mm, resulting in an expected surface roughness of about 0.5 mm for single track deposits. The printing process makes use of a Gas Metal Arc Welding (GMAW) and industrial multi-axis ABB robots.

The column has been manufactured at the MX3D facilities in Amsterdam using the same process parameters as the ones adopted to realize the specimens tested (Table 1). Table 4 provides the fabrication parameters in terms of effective layer height, printing time and actual weight.

Fabrication parameters	**Value**
Layer height	0.95 mm – 1.15 mm
Printing time	60 – 70 hours

Printed weight	26.50 kg

Table 4: Fabrication parameters.

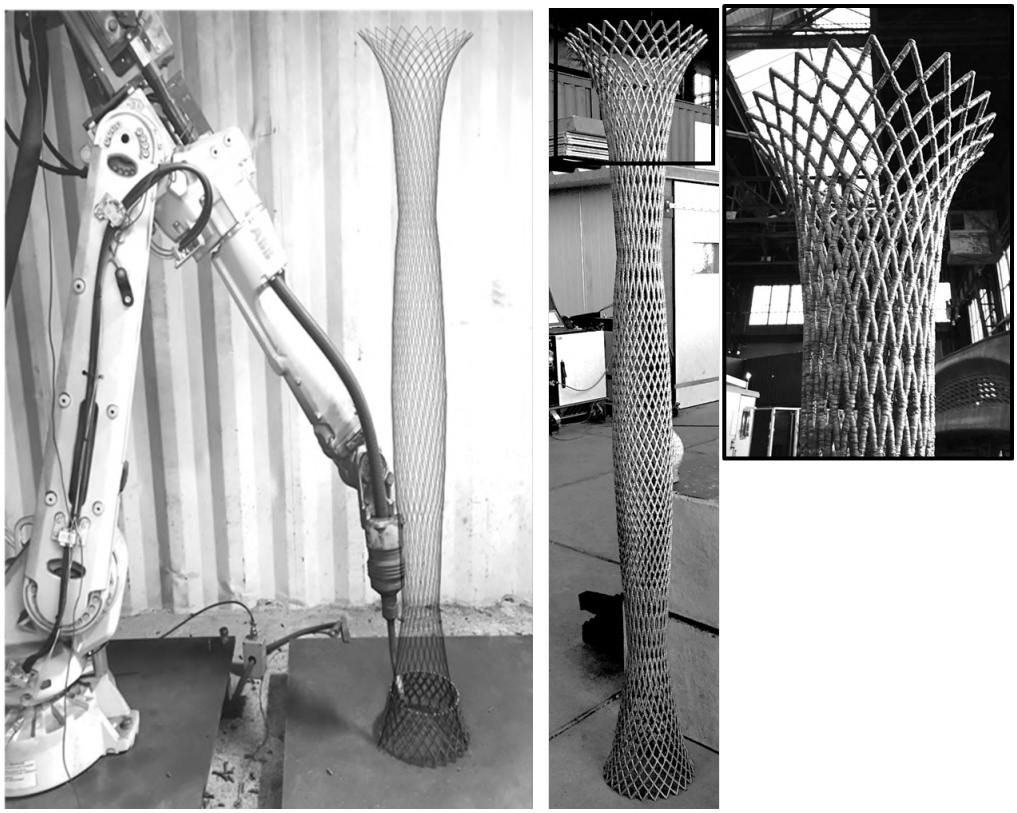

(a)

(b)

Figure 16: (a) Manufacturing of the designed diagrid column through WAAM process; (b) zoom of the top part.

The printed outcome has been presented at "The Big 5- International Building and Construction" show, held in Dubai from November 25th till November 28th 2018, as a showcase of the possibilities offered by metal 3D printing to create innovative forms and aesthetically appealing structures. The tree-like shape of the final diagrid column is particularly suitable for support of outdoor lightweight structures, such as tree-houses (Figure 17).

Figure 17: Application of the designed diagrid column as support for tree-houses.

Conclusions

The research presents the overarching design process from the concept to the fabrication of a diagrid column realized using Wire-and-Arc Additive Manufacturing (WAAM) technology. It represents an

example of a fully-engineered structure based on the circular integration of information coming from material characterization and manufacturing technology, architectural shapes and computational structural design and analysis. Among various metal AM technologies, WAAM has been employed for its high-speed printing capabilities, making it adequate to realize large-scaled free forms and shapes without ideally almost any constraints in terms of geometry and dimensions.

The experimental results from the geometrical and mechanical characterization of "dot-by-dot" WAAM rods indicate that the geometrical imperfections inherent of the printing process (cross-sectional variation and surface roughness) and the values of the key material properties (Young's modulus, yielding and tensile strength and ductility) are adequate for structural engineering applications.

The proposed computational design workflow accounts for the specific features of the WAAM strategy adopted, thus avoiding the need of an iterative design necessary to meet the manufacturing constraints when using conventional design approaches. The final design encompasses the manufacturing constraints proper of WAAM dot-by-dot printing strategy, ensuring sufficient structural performances under service load. Detailed study of the structural behavior of the final design compared with a uniform cylinder further proves that the solution proposed has reduced weight and overall better structural performances under compressive load with respect to a uniform diagrid cylinder.

The designed diagrid column has been then fabricated at MX3D and presented at "The Big 5 – International Building and Construction" 2018.

This first example of cohesive digital fabrication process from the computational design to the realization of a metal 3D-printed structural member is intended to pave the way towards a new generation of structures. Indeed, this innovative manufacturing technology would allow for novel forms and shapes, using advanced parametric design, fully engineered through WAAM process, whose properties in terms of both geometrical accuracy and printed material mechanical properties have been tested and certified.

On the other hand, the efficient use of this technology in the construction field would also require substantial advancements towards new automatized printing systems.

As such, the long-term perspective of the research is two-fold. From the characterization of the printed outcomes, experimental research should be carried out to improve the accuracy of the printing process, thus reducing the imperfections (both geometrical and mechanical) in the printed outcomes. To this aim, ad-hoc calibrated partial factors and design values of the key material properties are requested for structural design purposes. From the automation in construction, the development of a

fully integrated design/manufacturing process would bring this advanced technology for on-site construction. To this aim, the long-term vision will be the development of a mobile robotic system able to print and move on the structure to be constructed on-site and composed by a swarm of small robot-printers.

Acknowledgements

The support of Dutch company MX3D held in Amsterdam is gratefully acknowledged for giving the additive-manufactured elements tested.

The authors acknowledge the work done by Marcello Natalini to realize the renders for the diagrid columns.

The authors acknowledge the work done by Dr. Valentina Alena Girelli for the 3D scan acquisition of the specimens.

The research has been partially financed by the research project "Autor3dicolari", funded by University of Bologna within the call Almaidea2017.

Authors' contribution

Vittoria Laghi: Conceptualization, Investigation, Formal analysis, Writing – Original draft; Michele Palermo: Conceptualization, Visualization, Writing – Original draft; Giada Gasparini: Supervision, Writing – Reviewing and Editing; Tomaso Trombetti: Conceptualization, Supervision.

References

[1] W. Addis, Building: 3000 years of design engineering and construction., London: Phaidon, 2007.

[2] M. Carpo, The digital turn in architecture 1992-2012, John Wiley & Sons, 2013.

[3] S. Adriaenssens, P. Block, D. Veenendaal, C. Williams, Shell structures for architecture: form finding and optimization, Routledge, 2014.

[4] B. Khoshnevis, Automated construction by contour crafting - Related robotics and information technologies, in: Autom. Constr., 2004. https://doi.org/10.1016/j.autcon.2003.08.012.

[5] M. Attaran, The rise of 3-D printing: The advantages of additive manufacturing over traditional manufacturing, Bus. Horiz. (2017). https://doi.org/10.1016/j.bushor.2017.05.011.

[6] C.L. Thomas, T.M. Gaffney, S. Kaza, C.H. Lee, Rapid prototyping of large scale aerospace structures, in: 1996 IEEE Aerosp. Appl. Conf., 1998: pp. 219–230.

[7] B. Song, X. Zhao, S. Li, C. Han, Q. Wei, S. Wen, J. Liu, Y. Shi, Differences in microstructure and properties between selective laser melting and traditional manufacturing for fabrication of metal parts: A review, Front. Mech. Eng. 10 (2015) 111–125. https://doi.org/10.1007/s11465-015-0341-2.

[8] Y. Song, Y. Yan, R. Zhang, D. Xu, F. Wang, Manufacture of the die of an automobile deck part based on rapid prototyping and rapid tooling technology, J. Mater. Process. Technol. (2002). https://doi.org/10.1016/S0924-0136(01)01165-7.

[9] J. Giannatsis, V. Dedoussis, Additive fabrication technologies applied to medicine and health care: A review, Int. J. Adv. Manuf. Technol. 40 (2009) 116–127. https://doi.org/10.1007/s00170-007-1308-1.
[10] R. Naboni, L. Breseghello, A. Kunic, Multi-scale design and fabrication of the Trabeculae Pavilion, Addit. Manuf. 27 (2019) 305–317. https://doi.org/10.1016/j.addma.2019.03.005.
[11] Branch technology, (n.d.).
[12] AI Build, (n.d.).
[13] G. Vantyghem, W. De Corte, E. Shakour, O. Amir, 3D printing of a post-tensioned concrete girder designed by topology optimization, Autom. Constr. 112 (2020) 103084. https://doi.org/10.1016/j.autcon.2020.103084.
[14] A. Anton, A. Yoo, P. Bedarf, L. Reiter, T. Wangler, B. Dillenburger, Vertical Modulations: Computational design for concrete 3D printed columns, (2019). https://www.research-collection.ethz.ch:443/handle/20.500.11850/381686 (accessed May 27, 2020).
[15] S. Galjaard, S. Hofman, S. Ren, New Opportunities to Optimize Structural Designs in Metal by Using Additive Manufacturing, in: P. Block, J. Knippers, N.J. Mitra, W. Wang (Eds.), Adv. Archit. Geom. 2014, Springer International Publishing, Cham, 2015: pp. 79–93.
[16] MX3D Webpage, (n.d.). www.mx3d.com.
[17] T. Feucht, J. Lange, B. Waldschmitt, A.-K. Schudlich, M. Klein, M. Oechsner, Welding Process for the Additive Manufacturing of Cantilevered Components with the WAAM BT - Advanced Joining Processes, in: L.F.M. da Silva, P.A.F. Martins, M.S. El-Zein (Eds.), Springer Singapore, Singapore, 2020: pp. 67–78. https://doi.org/10.1007/978-981-15-2957-3_5.
[18] X. Zhang, K. Wang, Q. Zhou, J. Ding, S. Ganguly, G. Marzio, D. Yang, X. Xu, P. Dirisu, S.W. Williams, Microstructure and mechanical properties of TOP-TIG-wire and arc additive manufactured super duplex stainless steel (ER2594), Mater. Sci. Eng. A. 762 (2019) 138097. https://doi.org/10.1016/j.msea.2019.138097.
[19] J.J. Lewandowski, M. Seifi, Metal Additive Manufacturing: A Review of Mechanical Properties, Annu. Rev. Mater. Res. 46 (2016) 151–186. https://doi.org/10.1146/annurev-matsci-070115-032024.
[20] J. Gu, B. Cong, J. Ding, S.W. Williams, Y. Zhai, Wire+Arc Additive Manufacturing of Aluminium, SFF Symp. Austin Texas. (2014) 451–458.
[21] K. Oyama, S. Diplas, M. M'hamdi, A.E. Gunnæs, A.S. Azar, Heat source management in wire-arc additive manufacturing process for Al-Mg and Al-Si alloys, Addit. Manuf. 26 (2019) 180–192. https://doi.org/10.1016/j.addma.2019.01.007.
[22] C. V. Haden, G. Zeng, F.M. Carter, C. Ruhl, B.A. Krick, D.G. Harlow, Wire and arc additive manufactured steel: Tensile and wear properties, Addit. Manuf. 16 (2017) 115–123. https://doi.org/10.1016/j.addma.2017.05.010.
[23] J. Ge, J. Lin, Y. Chen, Y. Lei, H. Fu, Characterization of wire arc additive manufacturing 2Cr13 part: Process stability, microstructural evolution, and tensile properties, J. Alloys Compd. 748 (2018) 911–921. https://doi.org/10.1016/j.jallcom.2018.03.222.
[24] A. Queguineur, G. Rückert, F. Cortial, J.Y. Hascoët, Evaluation of wire arc additive manufacturing for large-sized components in naval applications, Weld. World. 62 (2018) 259–266. https://doi.org/10.1007/s40194-017-0536-8.
[25] W. Wu, J. Xue, L. Wang, Z. Zhang, Y. Hu, C. Dong, Forming process, microstructure, and mechanical properties of thin-walled 316L stainless steel using speed-cold-welding additive manufacturing, Metals (Basel). 9 (2019). https://doi.org/10.3390/met9010109.
[26] L. Wang, J. Xue, Q. Wang, Correlation between arc mode, microstructure, and mechanical properties during wire arc additive manufacturing of 316L stainless steel, Mater. Sci. Eng. A. 751 (2019) 183–190. https://doi.org/10.1016/j.msea.2019.02.078.
[27] Y. Fu, H. Zhang, G. Wang, H. Wang, Investigation of mechanical properties for hybrid deposition and micro-rolling of bainite steel, J. Mater. Process. Technol. 250 (2017) 220–227. https://doi.org/10.1016/j.jmatprotec.2017.07.023.
[28] G. Posch, K. Chladil, H. Chladil, Material properties of CMT—metal additive manufactured duplex stainless steel blade-like geometries, Weld. World. 61 (2017) 873–882. https://doi.org/10.1007/s40194-017-0474-5.
[29] X. Zhang, Q. Zhou, K. Wang, Y. Peng, J. Ding, J. Kong, S. Williams, Study on microstructure and tensile properties of high nitrogen Cr-Mn steel processed by CMT wire and arc additive manufacturing,

Mater. Des. 166 (2019) 107611. https://doi.org/10.1016/j.matdes.2019.107611.
[30] T. DebRoy, H.L. Wei, J.S. Zuback, T. Mukherjee, J.W. Elmer, J.O. Milewski, A.M. Beese, A. Wilson-Heid, A. De, W. Zhang, Additive manufacturing of metallic components – Process, structure and properties, Prog. Mater. Sci. 92 (2018) 112–224. https://doi.org/10.1016/j.pmatsci.2017.10.001.
[31] N. Rodriguez, L. Vázquez, I. Huarte, E. Arruti, I. Tabernero, P. Alvarez, Wire and arc additive manufacturing: a comparison between CMT and TopTIG processes applied to stainless steel, Weld. World. 62 (2018) 1083–1096. https://doi.org/10.1007/s40194-018-0606-6.
[32] L. Ji, J. Lu, C. Liu, C. Jing, H. Fan, S. Ma, Microstructure and mechanical properties of 304L steel fabricated by arc additive manufacturing, MATEC Web Conf. 128 (2017). https://doi.org/10.1051/matecconf/201712803006.
[33] T.A. Rodrigues, V. Duarte, J.A. Avila, T.G. Santos, R.M. Miranda, J.P. Oliveira, Wire and arc additive manufacturing of HSLA steel: Effect of thermal cycles on microstructure and mechanical properties, Addit. Manuf. 27 (2019) 440–450. https://doi.org/10.1016/j.addma.2019.03.029.
[34] C. Shen, Z. Pan, D. Cuiuri, B. Dong, H. Li, In-depth study of the mechanical properties for Fe3Al based iron aluminide fabricated using the wire-arc additive manufacturing process, Mater. Sci. Eng. A. 669 (2016) 118–126. https://doi.org/10.1016/j.msea.2016.05.047.
[35] B. Wu, Z. Pan, D. Ding, D. Cuiuri, H. Li, Z. Fei, The effects of forced interpass cooling on the material properties of wire arc additively manufactured Ti6Al4V alloy, J. Mater. Process. Technol. (2018). https://doi.org/10.1016/j.jmatprotec.2018.03.024.
[36] J. Gu, X. Wang, J. Bai, J. Ding, S. Williams, Y. Zhai, K. Liu, Deformation microstructures and strengthening mechanisms for the wire+arc additively manufactured Al-Mg4.5Mn alloy with inter-layer rolling, Mater. Sci. Eng. A. (2018). https://doi.org/10.1016/j.msea.2017.11.113.
[37] B. Wu, Z. Pan, D. Ding, D. Cuiuri, H. Li, J. Xu, J. Norrish, A review of the wire arc additive manufacturing of metals: properties, defects and quality improvement, J. Manuf. Process. (2018). https://doi.org/10.1016/j.jmapro.2018.08.001.
[38] M. Köhler, S. Fiebig, J. Hensel, K. Dilger, Wire and arc additive manufacturing of aluminum components, Metals (Basel). 9 (2019) 1–9. https://doi.org/10.3390/met9050608.
[39] K.S. Derekar, A review of wire arc additive manufacturing and advances in wire arc additive manufacturing of aluminium, Mater. Sci. Technol. (United Kingdom). 34 (2018) 895–916. https://doi.org/10.1080/02670836.2018.1455012.
[40] J. Gu, X. Wang, J. Bai, J. Ding, S. Williams, Y. Zhai, K. Liu, Deformation microstructures and strengthening mechanisms for the wire+arc additively manufactured Al-Mg4.5Mn alloy with inter-layer rolling, Mater. Sci. Eng. A. 712 (2018) 292–301. https://doi.org/10.1016/j.msea.2017.11.113.
[41] J. V. Gordon, C. V. Haden, H.F. Nied, R.P. Vinci, D.G. Harlow, Fatigue crack growth anisotropy, texture and residual stress in austenitic steel made by wire and arc additive manufacturing, Mater. Sci. Eng. A. 724 (2018) 431–438. https://doi.org/10.1016/j.msea.2018.03.075.
[42] J.R. Hönnige, P.A. Colegrove, S. Ganguly, E. Eimer, S. Kabra, S. Williams, Control of residual stress and distortion in aluminium wire + arc additive manufacture with rolling, Addit. Manuf. 22 (2018) 775–783. https://doi.org/10.1016/j.addma.2018.06.015.
[43] Z. Qi, B. Cong, B. Qi, G. Zhao, J. Ding, Properties of wire + arc additively manufactured 2024 aluminum alloy with different solution treatment temperature, Mater. Lett. 230 (2018) 275–278. https://doi.org/10.1016/j.matlet.2018.07.144.
[44] E.M. Ryan, T.J. Sabin, J.F. Watts, M.J. Whiting, The influence of build parameters and wire batch on porosity of wire and arc additive manufactured aluminium alloy 2319, J. Mater. Process. Technol. 262 (2018) 577–584. https://doi.org/10.1016/j.jmatprotec.2018.07.030.
[45] X. Xu, S. Ganguly, J. Ding, S. Guo, S. Williams, F. Martina, Microstructural evolution and mechanical properties of maraging steel produced by wire + arc additive manufacture process, Mater. Charact. 143 (2018) 152–162. https://doi.org/10.1016/j.matchar.2017.12.002.
[46] X. Fang, L. Zhang, G. Chen, X. Dang, K. Huang, L. Wang, B. Lu, Correlations between microstructure characteristics and mechanical properties in 5183 aluminium alloy fabricated by wire-arc additive manufacturing with different arc modes, Materials (Basel). 11 (2018). https://doi.org/10.3390/ma11112075.
[47] Z. Qi, B. Qi, B. Cong, R. Zhang, Microstructure and mechanical properties of wire + arc additively manufactured Al-Mg-Si aluminum alloy, Mater. Lett. 233 (2018) 348–350.

https://doi.org/10.1016/j.matlet.2018.09.048.
[48] C. Zhang, Y. Li, M. Gao, X. Zeng, Wire arc additive manufacturing of Al-6Mg alloy using variable polarity cold metal transfer arc as power source, Mater. Sci. Eng. A. 711 (2018) 415–423. https://doi.org/10.1016/j.msea.2017.11.084.
[49] E.M. Ryan, On Wire and Arc Additive Manufacture of Aluminium, (2018).
[50] G. Marinelli, F. Martina, S. Ganguly, S. Williams, H. Lewtas, D. Hancock, S. Mehraban, N. Lavery, Microstructure and thermal properties of unalloyed tungsten deposited by Wire + Arc Additive Manufacture, J. Nucl. Mater. (2019). https://doi.org/10.1016/j.jnucmat.2019.04.049.
[51] C. Buchanan, L. Gardner, Metal 3D printing in construction: A review of methods, research, applications, opportunities and challenges, Eng. Struct. 180 (2019) 332–348. https://doi.org/10.1016/j.engstruct.2018.11.045.
[52] V. Laghi, M. Palermo, G. Gasparini, V.A. Girelli, T. Trombetti, Experimental results for structural design of Wire-and-Arc Additive Manufactured stainless steel members, J. Constr. Steel Res. (2019).
[53] V. Laghi, M. Palermo, L. Tonelli, G. Gasparini, L. Ceschini, T. Trombetti, Tensile properties and microstructural features of 304L austenitic stainless steel produced by wire-and-arc additive manufacturing, Int. J. Adv. Manuf. Technol. (2020) 3693–3705. https://doi.org/10.1007/s00170-019-04868-8.
[54] V. Laghi, M. Palermo, G. Gasparini, V.A. Girelli, T. Trombetti, Geometrical characterization of Wire-and-Arc Additive Manufactured steel elements, VBRI Press Adv. Mater. Lett. 10 (2019) 695–699.
[55] Z. Wang, T.A. Palmer, A.M. Beese, Effect of processing parameters on microstructure and tensile properties of austenitic stainless steel 304L made by directed energy deposition additive manufacturing, Acta Mater. 110 (2016) 226–235. https://doi.org/10.1016/j.actamat.2016.03.019.
[56] I.S. Kim, K.J. Son, Y.S. Yang, P.K.D.V. Yaragada, Sensitivity analysis for process parameters in GMA welding processes using a factorial design method, Int. J. Mach. Tools Manuf. 43 (2003) 763–769. https://doi.org/10.1016/S0890-6955(03)00054-3.
[57] K. Guan, Z. Wang, M. Gao, X. Li, X. Zeng, Effects of processing parameters on tensile properties of selective laser melted 304 stainless steel, Mater. Des. 50 (2013) 581–586. https://doi.org/10.1016/j.matdes.2013.03.056.
[58] M. Liberini, A. Astarita, G. Campatelli, A. Scippa, F. Montevecchi, G. Venturini, M. Durante, L. Boccarusso, F.M.C. Minutolo, A. Squillace, Selection of Optimal Process Parameters for Wire Arc Additive Manufacturing, in: Procedia CIRP, 2017. https://doi.org/10.1016/j.procir.2016.06.124.
[59] J. Xiong, Y. Li, R. Li, Z. Yin, Influences of process parameters on surface roughness of multi-layer single-pass thin-walled parts in GMAW-based additive manufacturing, J. Mater. Process. Technol. (2018). https://doi.org/10.1016/j.jmatprotec.2017.09.020.
[60] M. Dinovitzer, X. Chen, J. Laliberte, X. Huang, H. Frei, Effect of wire and arc additive manufacturing (WAAM) process parameters on bead geometry and microstructure, Addit. Manuf. 26 (2019) 138–146. https://doi.org/10.1016/j.addma.2018.12.013.
[61] S.K. Joosten, Printing a stainless steel bridge: an exploration of structural properties of stainless steel additive manufactured for civil engineering purposes, University of Technology Delft, 2015.
[62] G.S. Van Bolderen, Exploration of stability of 3D-printed steel members, University of Technology Delft, 2017.
[63] Rhinoceros 5, (n.d.). www.rhino3d.com.
[64] Oerlikon, (n.d.). https://www.oerlikon.com/en/.
[65] European Committee for Standardization (CEN), EN 1993 1-4: Eurocode 3 - Design of steel structures, part 1-4: General rules, supplementary rules for stainless steel, (2015).
[66] J.B. Keller, The shape of the strongest column, Arch. Ration. Mech. Anal. 5 (1960) 275–285. https://doi.org/10.1007/BF00252909.
[67] A. Bejan, Shape and structure, from engineering to nature, Cambridge University Press, 2000.
[68] S. Bektas, Design of hyperboloid structures, J. Archit. Res. Dev. 1 (2017).
[69] M. Beckh, Hyperbolic structures: Shukhov's lattice towers-forerunners of modern lightweight construction, John Wiley & Sons, 2015.
[70] S.N. Krivoshapko, Static, vibration, and buckling analyses and applications to one-sheet hyperboloidal shells of revolution, Appl. Mech. Rev. 55 (2002) 241–269. https://doi.org/10.1115/1.1470479.
[71] Grasshopper, (n.d.). www.grasshopper3d.com.

[72] Karamba3D, (n.d.). www.karamba3d.com.
[73] European Committee for Standardization (CEN), EN 1990: Eurocode 0 - Basis of Structural Design, (2002).
[74] SAP2000, (n.d.). www.csiamerica.com/products/sap2000.
[75] K.S. Moon, J.J. Connor, J.E. Fernandez, Diagrid structural systems for tall buildings: Characteristics and methodology for preliminary design, Struct. Des. Tall Spec. Build. 16 (2007) 205–230. https://doi.org/10.1002/tal.311.
[76] W. Zhou, Z. Cao, J. Zhang, Experiment and analysis on reinforced concrete spatial connection in diagrid tube, Struct. Des. Tall Spec. Build. 25 (2016) 179–192. https://doi.org/10.1002/tal.1234.
[77] G.M. Montuori, E. Mele, G. Brandonisio, A. De Luca, Geometrical patterns for diagrid buildings: Exploring alternative design strategies from the structural point of view, Eng. Struct. 71 (2014) 112–127. https://doi.org/10.1016/j.engstruct.2014.04.017.
[78] E. Mele, M. Toreno, G. Brandonisio, A. De Luca, Diagrid structures for tall buildings: case studies and design considerations, Struct. Des. Tall Spec. Build. 23 (2014) 124–145. https://doi.org/10.1002/tal.